PROCEEDINGS OF SPIE

SPIEDigitalLibrary.org/conference-proceedings-of-spie

Sensitivity study of transverse translation diverse phase retrieval for freeform metrology

Aaron Michalko, James R. Fienup

Aaron Michalko, James R. Fienup, "Sensitivity study of transverse translation diverse phase retrieval for freeform metrology," Proc. SPIE 10742, Optical Manufacturing and Testing XII, 107420T (14 September 2018); doi: 10.1117/12.2321212



Event: SPIE Optical Engineering + Applications, 2018, San Diego, California, United States

Sensitivity Study of Transverse Translation Diverse Phase Retrieval for Freeform Metrology

Aaron M. Michalko and James R. Fienup University of Rochester, Rochester, NY, USA

ABSTRACT

Transverse translation-diverse phase retrieval (TTDPR), a ptychographic wavefront-sensing technique, is a viable method for optical surface metrology due to its relatively simple hardware requirements, flexibility, and high demonstrated accuracy in other fields. In TTDPR, a subaperture illumination pattern is scanned across an optic under test, and the reflected intensity is gathered on an array detector near focus. A nonlinear optimization algorithm is used to reconstruct the wavefront aberration at the test surface, from which we can solve for surface error, using intensity patterns from multiple scan positions. TTDPR is an advantageous method for aspheric and freeform metrology, because measurements can be performed without null optics. We report on a sensitivity analysis of TTDPR using simulations of a freeform concave mirror measurement. Simulations were performed to test TTDPR algorithmic performance as a function of various parameters, including detector SNR and position uncertainty of the illumination.

Keywords: Phase Retrieval, Surface Metrology, Freeform Metrology, Wavefront Sensing

1. INTRODUCTION

Freeform optical surfaces, though attractive to optical designers for their flexibility and aberration-correcting capabilities, can pose a significant challenge for optical metrology. Unlike conic surfaces, freeforms generally do not possess a stigmatic imaging configuration which would facilitate an interferometric null test. Rather, slope departure of a freeform shape from a base sphere can create unresolvable test fringes on the detector, in addition to introducing retrace errors. To overcome these challenges, additional optics may be introduced, such as a computer-generated hologram or custom null configuration, or subaperture stitching may be used. Often, these methods tend to be expensive and require complicated additional hardware to take a measurement. We are interested in an alternative metrology approach suitable for freeform surface characterization with significantly reduced hardware requirements and associated cost.

One suitable technique is transverse translation-diverse phase retrieval (TTDPR), a ptychographic method of image-based wavefront sensing.^{3–6} TTDPR is an attractive technique for optical surface metrology, particularly concave surface metrology, due to its relatively simple hardware requirements.^{7,8} Using TTDPR, measurements of concave surfaces may only require a source, a translating mask, and an array detector. A TTDPR measurement does not require additional reference or imaging optics, reducing the cost and uncertainties associated with manufacturing and calibrating those optics. Additionally, TTDPR does not suffer from retrace errors when measuring an aspheric wavefront, and is suitable to measure aspheric and freeform optics without needing additional null optics.

In this paper, we discuss the application of TTDPR for freeform optical testing, focusing on concave optical surface testing. We first describe the TTDPR method in Sec. 2. Later, in Sec. 3, we report on the results of computer simulations used to explore TTDPR algorithmic performance in the presence of realistic testing conditions.

2. TTDPR METHOD

TTDPR is a method of estimating a complex field of interest using measured intensities in a plane near the focus. Like other methods of phase retrieval, TTDPR involves optimizing the agreement between measured intensities with computer-propagated intensity predictions. Intensities are predicted by digitally propagating an estimate of the field of interest to a simulated measurement plane. In the context of optical systems testing, the field of interest is often located in an exit pupil, where the phase can be interpreted as a transmitted wavefront error,

Optical Manufacturing and Testing XII, edited by Ray Williamson, Dae Wook Kim, Rolf Rascher, Proc. of SPIE Vol. 10742, 107420T ⋅ © 2018 SPIE CCC code: 0277-786X/18/\$18 ⋅ doi: 10.1117/12.2321212

and can be used to diagnose system errors and possibly perform wavefront correction. The estimate of the field is iteratively updated to optimize the agreement between the predicted intensities and the measured ones, until a final prediction of the full complex field is obtained. In TTDPR, data diversity is achieved by including a subaperture illumination pattern which is scanned across the exit pupil. The scanning subaperture is sized to produce well-sampled intensities, where sampling is expressed in terms of the sampling factor, Q:⁹

$$Q = \frac{\lambda z}{D\Delta_u}. (1)$$

where λ is the test wavelength, z is propagation distance, Δ_u is detector pixel pitch, and D is the physical diameter of the subaperture in the exit pupil. Q=2 corresponds to Nyquist-sampled intensities. By scanning the subaperture across the field of interest, we are able to take well-sampled measurements over a much larger effective diameter than would be possible using a full-aperture phase retrieval technique, such as defocus-diverse phase retrieval.

For transmitted wavefront testing of an optical element,³ the exit pupil may be defined in a plane just past the optic, and a physical translating subaperture structure can be placed directly in the exit pupil plane. However, for optical surface testing, we treat an optical surface as an effective pupil, and instead take measurements in reflection. Because a physical subaperture structure placed at or near the surface may obscure portions of the reflected beam or possibly damage the surface, translating subaperture illumination can instead be achieved by projecting an illumination pattern onto the surface under test.⁸ We reconstruct the complex field in a plane near the surface, and use the reconstructed wavefront aberration to solve for surface deformations using our knowledge of the system geometry. This data interpretation is similar to the one made in interferometry; in both cases, measurements of wavefront error are used to calculate surface error, although the wavefront error measurements are taken in very different ways.

The basic TTDPR forward model is as follows. We begin by modeling a generalized exit pupil function of our test configuration

$$g(x_p, y_p) = |g(x_p, y_p)| \exp\left[\frac{i2\pi}{\lambda} W(x_p, y_p)\right]$$
(2)

where λ is the source wavelength and $W(x_p, y_p)$ is the unknown wavefront aberration we want to characterize, expressed in pupil coordinates, (x_p, y_p) , with units of length. $W(x_p, y_p)$ is interpreted as the optical path difference between the aberrated wavefront in the exit pupil and a reference sphere centered on an ideal image point. $W(x_p, y_p)$ is often parametrized using basis polynomials, such as Zernike polynomials, in order to efficiently model the dominant low-order surface figure errors expected from the optical fabrication process. However, aspheric and freeform optics are often fabricated using subaperture grinding, polishing, or turning techniques, which leave behind characteristic mid-spatial frequency (MSF) surface errors in addition to lower frequency figure errors. Zernike polynomials are limited in their ability to reconstruct MSF features with high accuracy, possibly requiring tens of thousands of terms. To avoid the requirement for very large numbers of basis polynomials, which could become computationally expensive, we adopt the following wavefront parametrization:

$$W(x_p, y_p) = \sum_{j} a_j Z_j(x_p, y_p) + [P(x_p, y_p) * K(x_p, y_p)]$$
(3)

where $Z_j(x_p, y_p)$ is the jth Zernike polynomials with weight a_j to model low-order wavefront errors. The function $P(x_p, y_p)$ is a point-by-point (PBP) varying phase, * denotes convolution, and $K(x_p, y_p)$ is a convolution kernel. By changing the width of $K(x_p, y_p)$, we can control the spatial frequency bandwidth of $W(x_p, y_p)$, allowing us to model MSF and higher spatial frequency features. The use of a convolution is an improvement over a PBP-only phase, which can be prone to algorithmic stagnation or overfitting. This convolution-based model is termed the method of sieves, and has been used in phase retrieval in other contexts.¹³

Next, we introduce a complex-valued, translating subaperture illumination function, $A_k(x_p, y_p)$. For each of k translated positions, the field transmitted through the exit pupil can be modeled by

$$g_k(x_n, y_n) = A_k(x_n, y_n)g(x_n, y_n).$$
 (4)

In some cases, we may assume that for each translation (x_k, y_k) , $A_k(x_p, y_p)$ undergoes a translation, i.e,

$$A_k(x_p, y_p) = A_k(x_p - x_k, y_p - y_k). (5)$$

Subsequently, Eq. (4) becomes

$$g_k(x_p, y_p) = A_k(x_p - x_k, y_p - y_k)g(x_p, y_p).$$
(6)

To accommodate non-integer values of x_k and y_k , bilinear interpolation⁵ was used in this work. Other methods, such as the Fourier shift theorem may also be used to calculate a non-integer shifted. Next, we model the field incident on the detector as

$$G(u,v) = \mathbf{P}[g_k(x_p, y_p)] \tag{7}$$

where P is an appropriate propagator. In this work, we assume that the field at the detector plane is related to the general pupil function through Fraunhofer propagation, which can be written in discrete form:

$$\mathbf{G}_{k}[m_{r}, m_{c}] \propto \sum_{n_{r}=0}^{N-1} \sum_{n_{c}=0}^{N-1} \mathbf{g}_{k}[n_{r}, n_{c}] \exp\left[-i2\pi \left(\frac{\Delta_{u} \Delta_{x}}{\lambda z_{o}}\right) (n_{c} m_{c} + n_{r} m_{r})\right]. \tag{8}$$

where $G[m_r, m_c]$ is the size $M \times M$ detector array with row and column indices $[m_r, m_c]$ and pixel pitch Δ_u , $g_k[n_r, n_c]$ is a size $N \times N$ pupil array with row and column indices $[n_r, n_c]$ and simulated pixel length Δ_x , and z_0 is the propagation distance from the center of the pupil to the center of the detector. We have dropped constant leading terms, as well as a leading quadratic phase which goes away in Eq. (9). The model for the detected intensity on the array detector is

$$I_k \propto |G_k|^2$$
. (9)

These simulated intensities are then compared to measured intensities, D_k , using a suitable error metric. We used a normalized gain and bias insensitive mean-squared error metric given by

$$E = \frac{\sum_{k} \sum_{m_r, m_c} \mathbf{w}_k [\mathbf{D}_k - (\alpha_k \mathbf{I}_k + \beta_k)]^2}{\sum_{k} \sum_{m_r, m_c} \mathbf{w}_k \mathbf{D}_k^2}$$
(10)

where w_k is a bad pixel map, and α_k and β_k can be calculated using Eq. (C3) in Ref. 5.

We are tasked with minimizing the value of E with respect to experimental parameters. For this work, optimization was performed using an L-BFGS optimizer.¹⁴ Gradients with respect to various test parameters were calculated using algorithmic differentiation techniques.^{5,15}

3. COMPUTER SIMULATIONS

A series of computer simulations were performed to probe the wavefront-sensing accuracy of TTDPR in realistic testing scenarios for freeform optics. These simulations were driven by the selection of a candidate freeform mirror: the secondary mirror from a three-mirror, freeform, thermal imager^{1,16,17}. Figure 1 illustrates the candidate measurement geometry. The mirror would be illuminated by a point source positioned near its nominal center of curvature, with reflected intensities recorded by an array detector downstream. A clipping mask placed between the source and freeform would create the subaperture illumination. The mirror would be tilted by a nominal angle β , which serves two purposes. First, it clears the reflected beam from obstruction by the mask or detector. Second, because the mirror sag is dominated by an astigmatic component, tilt may be used to partially null surface-induced aberrations and can be used to vary the magnitude of W. For computer simulations, ray trace software was used to simulate the mirror in the test configuration shown in Fig. 1. Simulations were performed based on two tilt angles, $\beta = 7^{\circ}$ and $\beta = 13.91^{\circ}$. $\beta = 7^{\circ}$ represents a test case in which we use tilt angle simply to avoid obscuration. $\beta = 13.91^{\circ}$ represents a case where we use tilt to null nominal surface-induced astigmatism.

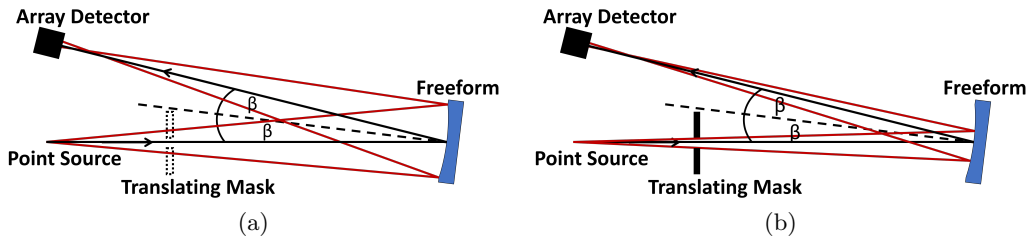


Figure 1: Test schematic for freeform surface measurement with (a) the translated mask removed and (b) the translating mask in place. The mirror is nominally tilted by an angle β .

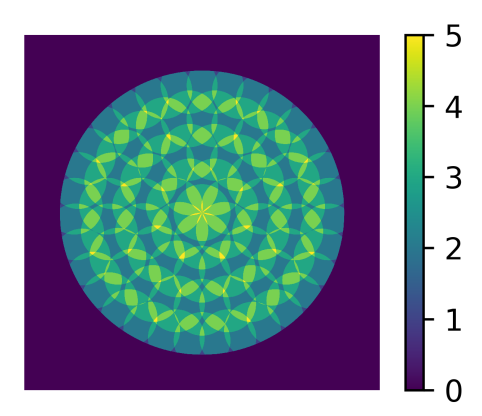


Figure 2: Superposition of subaperture positions. Colorbar value indicates the number of times an area of the pupil was sampled.

3.1 TTDPR On Noisy Data

First, simulations were performed to explore the effect of simulated detector noise on TTDPR accuracy. A series of wavefront aberrations were simulated based on a CODE V ray-trace model of the tilted freeform mirror with a tilt angle of $\beta = 7^{\circ}$. 36 nominal Zernike wavefront coefficients were generated using CODE V, and these coefficients were exported to a TTDPR algorithm and used as the a_i in Eq. (3) for simulating the wavefront from the ideal (nominal) surface under test. No additional PBP phase was simulated. This nominal wavefront aberration was defined over a circular clear aperture, and had a peak-to-valley (P-V) height of 305.4 λ and an RMS of 60.9λ , with piston, tip and tilt (PTT) removed, at the simulated test wavelength of $632.8 \,\mathrm{nm}$. To the nominal wavefront aberration, perturbations were added using a random superposition of 20 Zernike polynomials (through 5^{th} radial order), with 4.0 λ RMS departure from nominal. These perturbation represented unknown errors caused by fabrication defects. A translating circular subaperture with a diameter equal to 20% the underlying pupil diameter was modeled. In order to achieve good coverage over the entire simulated wavefront function, 77 translated positions were simulated, arranged in a concentric ring pattern as shown in Fig. 2. Nyquist-sampled intensities were modeled and detector noise was generated using a combined Gaussian and Poisson noise model, using 16 electron RMS Gaussian read noise and varying peak pixel photons. Ten simulations having different noise realizations were performed for each peak photoelectron level. In optimization, 35 Zernike polynomial coefficients were optimized (piston ignored) using the nominal wavefront as the starting guess. After optimization, the root mean squared wavefront-sensing error (RMS WFSE) was calculated between the reconstructed and true wavefronts to assess the accuracy of TTDPR. All other parameters except a_i were assumed known. Figure 3 shows the RMS WFSE v. peak pixel photons for the simulated cases. For cases with 10,000 peak photons or fewer, the algorithm could reliably converge with RMS error on the order of $\lambda/1000$, and $< \lambda/100$ RMS error was achievable with as few as 400 peak photons. These signal powers are easily obtainable in the lab, so we therefore expect detector noise alone to affect the accuracy of TTDPR very little in a laboratory testing environment.

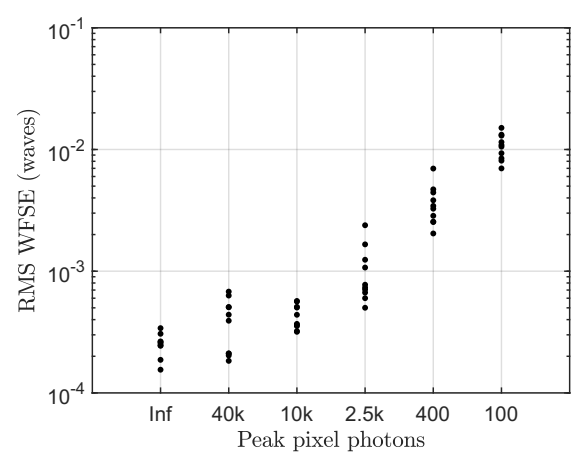


Figure 3: Residual root mean square wavefront sensing error (RMS WFSE) vs. peak pixel photons.

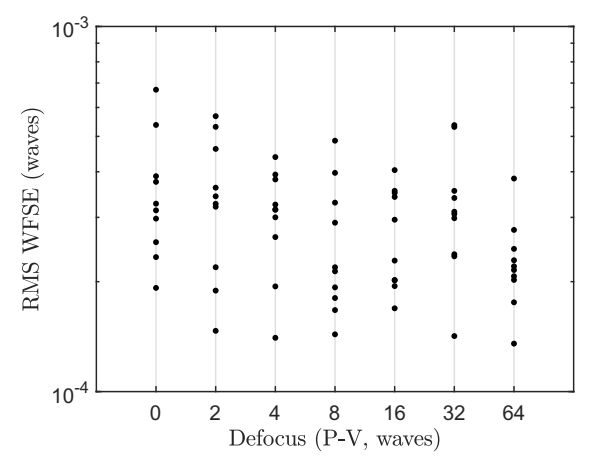
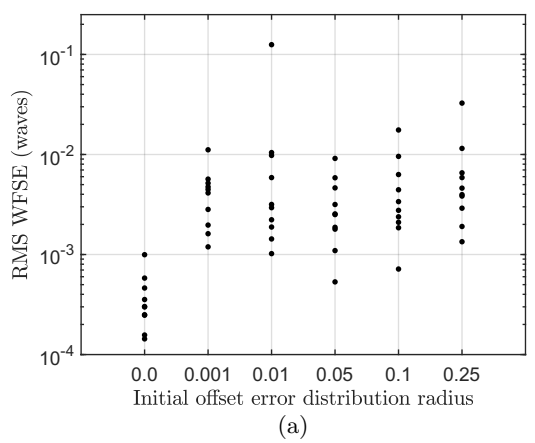


Figure 4: Residual RMS WFSE vs. known defocus. For a large range of known defocus values, phase was retrieval with sub $\lambda/1000$ RMS residual error.

3.2 TTDPR With Known Defocus

Next, TTDPR wavefront-sensing accuracy was tested in the presence of varying amounts of known defocus, because it has been shown that phase retrieval for wavefront sensing can sometimes benefit from the addition of defocus to the nominal wavefront. 18-21 For testing well-corrected optical systems, additional defocus spreads the otherwise narrow intensity distribution over a larger region on the detector, leading to a greater number of high-SNR pixels that contribute to E. However, in freeform optical testing, the measured PSFs are in general many times larger than the diffraction limit, due to the underlying surface shape of the optic and lack of a trivial null configuration. In order to test the performance of TTDPR with respect to known defocus, simulations were performed using the parameters described in Sec. 3.1, but for the fixed noise conditions of 16 electron RMS Gaussian read noise and 40k peak pixel photons. For each simulation, a known amount of Zernike defocus was added to the nominal wavefront. Defocus magnitudes ranging from 0 to 64 λ P-V were simulated. Such values could be attained in the lab by translating the detector along the optical axis or by inserting a weaklypowered optical element into the beampath. Figure 4 shows WFSE vs. Defocus for the simulations performed. RMS WFSE $< \lambda/1000$ was observed over the entire range of simulations with no strong functional dependence observed. This is most likely caused by the large aberration contribution of the nominal wavefront. Even with no additional defocus, the simulated intensities have energy spread over many pixels, contributing strongly to reducing the error metric.



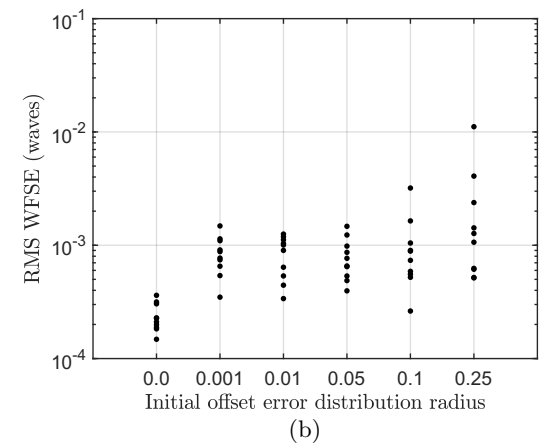


Figure 5: Residual RMS WFSE vs. size of initial offset error distribution, corresponding to mirror tilt angles of (a) $\beta = 7^{\circ}$ and (b) $\beta = 13.91^{\circ}$. Initial offset errors were drawn from a uniform random distribution over a disk, whose radius was specified as a fraction of the total subaperture width.

3.3 TTDPR with Subaperture Positioning Error

Next, the accuracy of TTDPR was explored with respect to errors in the position of the subaperture illumination. Errors in subaperture position may occur in the lab as a result of calibration errors, or systematic errors from the stages used to translate the moving mask. Joint retrieval of subaperture position along with wavefront error has been previously demonstrated using TTDPR for mildly aberrated systems.^{3,5,6,22} We are interested in how uncertainties in subaperture position will affect the freeform case, where aberrations are, in general, much larger.

For these simulations, wavefronts and data were again simulated according to the process described in Sec. 3.1 with 40k simulated peak pixel photons. However, for these simulations, the initial guess for each subaperture position was perturbed by a random offset. Random offset errors were drawn from a uniform distribution over a disk with a specified radius. The radius of this distribution varied from 0 to 25% the subaperture width. In optimization, 35 Zernike coefficients were first optimized with fixed (yet incorrect) translations. Next, all subaperture translations were optimized jointly with the wavefront coefficients. All other parameters except translations and coefficients were assumed known.

We were further interested in how TTDPR sensitivity may change depending on the magnitude of the nominal aberrations. In addition to the $\beta=7^{\circ}$ nominal wavefront aberration, we also performed simulations on the more well-corrected $\beta=13.91^{\circ}$ wavefront aberration, which had a 67.7 λ P-V and 15.9 λ RMS over the simulated area of interest with PTT removed.

Figure 5 shows WFSE v. subaperture offset error for both sets of simulations. Compared to Figs. 3 and 4, Fig. 5(a) shows a larger mean and variance of WFSE, with the worst case resulting in $\approx 0.12 \lambda$ RMS WFSE, [the uppermost point in Fig. 5(a)], which was found to be dominated by a linear phase error. Once the linear phase component had been removed from that result, the residual WFSE was reduced to 0.02λ . However, the ensemble performed well overall, with 54/60 cases resulting in $< 0.01 \lambda$ RMS WFSE. Fig. 5(b) shows lower overall error, with 59/60 cases resulting in $< 0.01 \lambda$ RMS WFSE. Although uncertainty in subaperture position we will cause additional uncertainty in the final wavefront reconstructions, these results show that successful retrievals are still possible with random offset errors up to 25% the subaperture diameter. In a testing environment, calibration should be performed to minimize these errors, but there are additional paths toward developing a more robust test in the presence of unknown offset errors. One may be developing a better optimization strategy, in which we more strictly control when and how the subaperture translations may vary in optimization.⁵ It may also be advantageous to introduce known amplitude structures in the optical aperture that would serve as position references for the translating illumination.

3.4 TTDPR With Errors in the Sampling Parameter

As shown in Eq. (8), simulated intensities were propagated using a discrete Fraunhofer propagation, which we recognize as a discrete Fourier transform (DFT). TTDPR performance was tested in the presence of errors in the DFT sampling parameter, α , given by

$$\alpha = \frac{\Delta_u \Delta_x}{\lambda z_0}. (11)$$

 α is the sampling (interpolation/scaling) parameter in the DFT, and must be selected to ensure that simulated intensities are not aliased by the wraparound nature of the DFT. α relates to Q by

$$\alpha = \frac{\Delta_x}{QD} \tag{12}$$

where D is the physical width of the subaperture illumination in the exit pupil. From a practical perspective, uncertainties in α are directly linked to uncertainties in physical experimental parameters. Therefore, an exploration of TTDPR performance in the presence of errors in α may help inform an error budget on the various physical terms contributing to Eq.(11). Previous work regarding α reconstruction demonstrated high accuracy, but dealt with 0.1 λ RMS wavefronts using defocus-diverse phase retrieval.²³ We are interested in the performance of TTDPR with highly aberrated wavefronts that we would expect from freeform testing. In this work, both the matrix-product DFT²⁴ and Chirp-z transform²³ were used instead of an FFT. This allows α to take on any value, rather than the value 1/N, where N is the number of pixels in the input array, the FFT constraint. For these simulations, wavefronts and data were again simulated according to the process in Sec. 3.1 with 40k peak photons. However, in these simulations, α was allowed to vary with optimization along with the 35 Zernike coefficients, and all other parameters were assumed known. Data were simulated using the true sampling parameter, α_{true} , but the starting guess, α_{init} , was perturbed by a prescribed amount relative to the truth. In these simulations, both α and coefficients a_i were jointly optimized from the start. After optimization, estimates of both the wavefront coefficients, as well as the sampling parameter, α_{rec} , were obtained, and RMS WFSE was calculated. Figures 6(a) and 6(b) show RMS WFSE vs. fractional error in the initial value of the sampling parameter, $|(\alpha_{init} - \alpha_{true})/\alpha_{true}|$. As shown in Fig. 6(a), the higher aberrated wavefront was more sensitive to errors in alpha, with 48/60 simulations resulting is RMS WFSE $< 0.01 \lambda$. For the less aberrated case, $\beta = 13.91^{\circ}$, 60/60 simulations resulted in RMS WFSE < 0.01 λ . In both cases, TTDPR performance did not appear to depend strongly on the specific value of α_{init} . To better understand these results, residual RMS WFSE was compared to fractional error in the reconstructed sampling parameter, $|(\alpha_{rec} - \alpha_{true})/\alpha_{true}|$, shown in Figs. 6(c) and 6(d). Fractional error in the reconstructed sampling parameter was found to be approximately proportional to RMS WFSE, especially for the case of $\beta = 7^{\circ}$ as shown in Fig. 6(c). A linear regression was calculated, and the data agree to the following model,

$$\left| \frac{\alpha_{rec} - \alpha_{true}}{\alpha_{true}} \right| = 64.84 (\text{RMS WFSE}) + 0.00053, \tag{13}$$

with $R^2 = 0.987$.

We can gain an intuition for this proportional error if we consider the phase retrieval system in terms of geometrical optics. According to geometrical optics, transverse ray aberration, and therefore geometrical spot size, is proportional to the magnitude of the wavefront aberration function. In the presence of large aberrations, such as the case with $\beta=7^{\circ}$, the shapes of the measured intensities are largely governed by geometrical effects. Because α acts as a DFT scaling parameter, an error in α may appear as if brightest intensity regions have been geometrically magnified. This, in turn, may lead to a local minima in optimization in which the error in α is "corrected" by a proportional change in the magnitude of the wavefront aberration. However, the intensities will also possess high spatial frequency features whose periodicity is dependent only on α , which appear only when diffraction is modeled. In the presence of large aberrations, those features can be orders of magnitude dimmer than the brightest intensity regions, so they may contribute relatively little to the nonlinear optimizer as it searches for a global minimum. Previous work regarding α reconstruction dealt with 0.1 λ RMS wavefronts, in which diffraction effects still contribute strongly to the shape of the measured intensities.²³ Furthermore, the data in Fig. 6(d), corresponding to a wavefront aberration function with 15.9 λ RMS (PTT removed), show

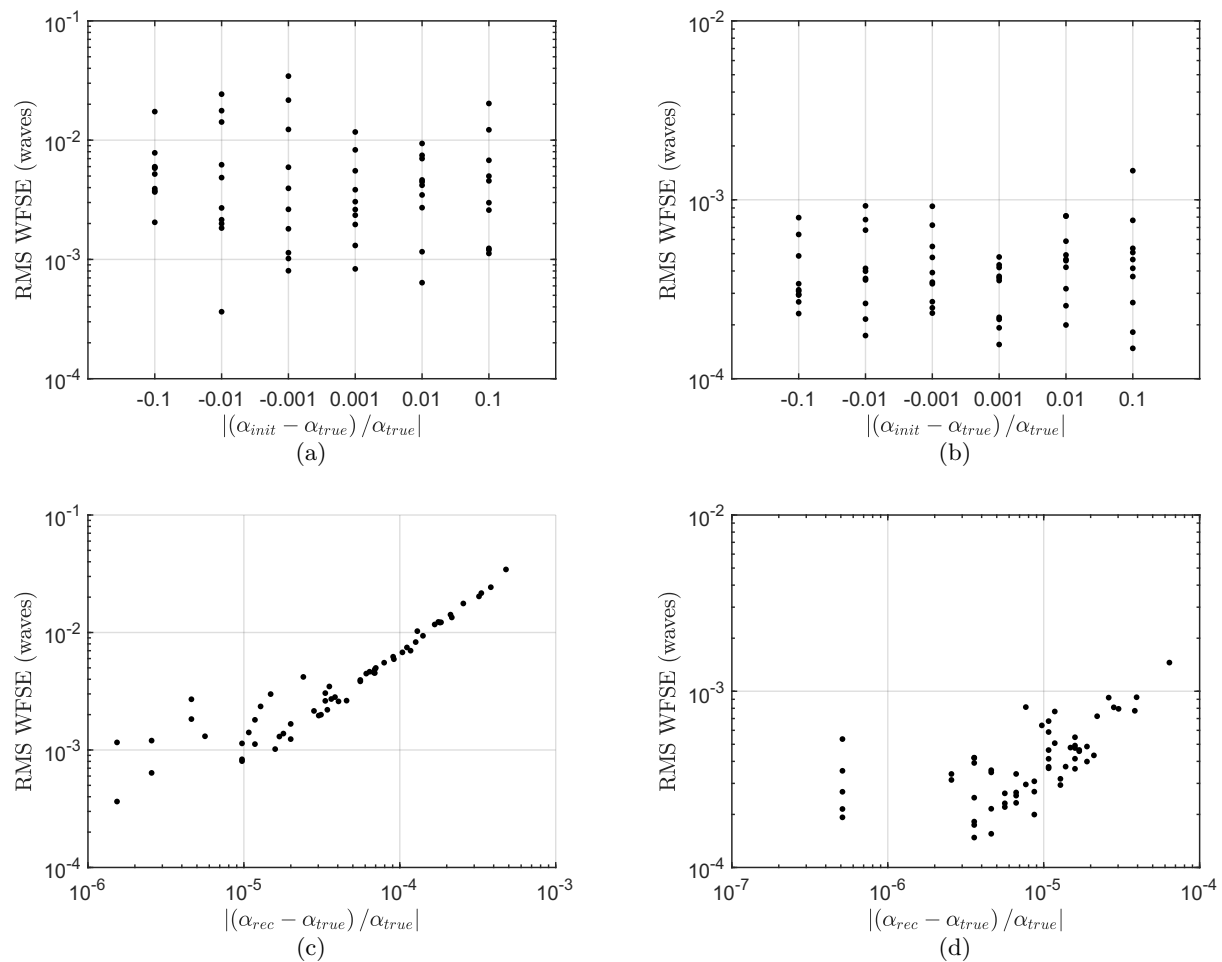


Figure 6: (a) RMS WFSE vs. error in the initial sampling parameter, $|(\alpha_{init} - \alpha_{true})/\alpha_{true}|$, corresponding to a mirror tilt angle of $\beta = 7^{\circ}$. RMS WFSE was calculated after optimization, in which the value of α was varied jointly with wavefront coefficients. (b) RMS WFSE vs. error in the initial sampling parameter, $|(\alpha_{init} - \alpha_{true})/\alpha_{true}|$, corresponding to a mirror tilt angle of $\beta = 13.91^{\circ}$. RMS WFSE was calculated after optimization, in which the value of α was varied jointly with wavefront coefficients. (c) RMS WFSE vs. error in the reconstructed sampling parameter, $|(\alpha_{rec} - \alpha_{true})/\alpha_{true}|$, for $\beta = 7^{\circ}$. These are the same set of RMS WFSE results as shown in Fig. 6(a), but compared against a different parameter. (d) RMS WFSE vs. error in the reconstructed sampling parameter, $|(\alpha_{rec} - \alpha_{true})/\alpha_{true}|$, for $\beta = 13.91^{\circ}$. These are the same set of RMS WFSE results as shown in Fig. 6(b), but compared against a different parameter.

lower overall WFSE overall and do not agree as well to a linear regression, suggesting that diffraction effects still contribute strongly to those intensities. If TTDPR is being used to test a highly aberrated wavefront, and error in α is a concern, the capture range of α retrieval may be improved by probing the system in ways that allow diffraction effects to be a more dominant contributor to the recorded intensities. One approach may be to take measure additional intensities with longer exposure times, where the brightest region is oversaturated, but the dimmer diffraction lobes have high SNR. A data mask can be applied in optimization to ignore the overexposed regions while fitting the dimmer ones. Alternatively, a second subaperture may be employed, such as a double-pinhole, which would create a modified double-slit arrangement. The resulting intensities should contain a fringe pattern with a spatial frequency that depends on α .

4. CONCLUSION

In this work, we have quantitatively explored the sensitivity of TTDPR, an image-based wavefront sensing technique, through simulations of a candidate freeform measurement. TTDPR algorithmic performance was tested with respect to detector SNR, measurement defocus, errors in subaperture offset position, and errors in the Fourier sampling parameter, with $< \lambda/100$ performance demonstrated in most cases. We are currently working to verify this method through the laboratory measurement of a concave freeform mirror.

ACKNOWLEDGMENTS

This research was supported by the NSF I/UCRC Center for Freeform Optics (IIP-1338877 and IIP-1338898).

REFERENCES

- 1. K. Fuerschbach, K. P. Thompson, and J. P. Rolland, "Interferometric measurement of a concave, ϕ -polynomial, zernike mirror," *Opt. Lett.* **39**, pp. 18–21, Jan 2014.
- 2. P. Murphy, G. Forbes, J. Fleig, P. Dumas, and M. Tricard, "Stitching interferometry: A flexible solution for surface metrology," *Opt. Photon. News* 14, pp. 38–43, May 2003.
- 3. G. R. Brady, M. Guizar-Sicairos, and J. R. Fienup, "Optical wavefront measurement using phase retrieval with transverse translation diversity," *Optics express* 17(2), pp. 624–639, 2009.
- 4. D. B. Moore and J. R. Fienup, "Subaperture translation estimation accuracy in transverse translation diversity phase retrieval," *Appl. Opt.* **55**, pp. 2526–2536, Apr 2016.
- 5. D. B. Moore and J. R. Fienup, "Ptychography for optical metrology with limited translation knowledge," *Appl. Opt.* **55**, pp. 4596–4610, Jun 2016.
- M. Guizar-Sicairos and J. R. Fienup, "Phase retrieval with transverse translation diversity: a nonlinear optimization approach," Opt. Express 16, pp. 7264–7278, May 2008.
- A. Michalko and J. R. Fienup, "Concave mirror measurement using transverse translation diverse phase retrieval," in Optical Design and Fabrication 2017 (Freeform, IODC, OFT), Optical Design and Fabrication 2017 (Freeform, IODC, OFT), p. OW2B.5, Optical Society of America, 2017.
- 8. A. M. Michalko and J. R. Fienup, "Transverse translation diverse phase retrieval using soft-edged illumination," *Optics Letters*, 2018.
- 9. G. R. Brady and J. R. Fienup, "Measurement range of phase retrieval in optical surface and wavefront metrology," *Appl. Opt.* **48**, pp. 442–449, Jan 2009.
- 10. J. Goodman, Introduction to Fourier Optics. Macmillan, 4 ed., 2016.
- 11. R. J. Noll, "Zernike polynomials and atmospheric turbulence*," J. Opt. Soc. Am. 66, pp. 207–211, Mar 1976.
- 12. C. J. E. Zahra Hosseinimakarem, Angela D. Davies, "Zernike polynomials for mid-spatial frequency representation on optical surfaces," *Proc.SPIE* **9961**, pp. 9961 9961 18, 2016.
- 13. S. T. Thurman, R. T. DeRosa, and J. R. Fienup, "Amplitude metrics for field retrieval with hard-edged and uniformly illuminated apertures," J. Opt. Soc. Am. A 26, pp. 700–709, Mar 2009.
- 14. C. Zhu, R. Byrd, P. Lu, and J. Nocedal, "Algorithm 778: L-BFGS-B: Fortran subroutines for large-scale bound-constrained optimization," *ACM Trans. Math. Softw.* **23**, pp. 550–560, 12 1997.
- 15. A. S. Jurling and J. R. Fienup, "Applications of algorithmic differentiation to phase retrieval algorithms," *J. Opt. Soc. Am. A* **31**, pp. 1348–1359, Jul 2014.
- 16. K. Fuerschbach, J. P. Rolland, and K. P. Thompson, "A new family of optical systems employing ϕ -polynomial surfaces," Opt. Express 19, pp. 21919–21928, Oct 2011.
- 17. K. Fuerschbach, G. E. Davis, K. P. Thompson, and J. P. Rolland, "Assembly of a freeform off-axis optical system employing three φ-polynomial Zernike mirrors," *Opt. Lett.* **39**, pp. 2896–2899, May 2014.
- 18. J. R. Fienup, B. J. Thelen, R. G. Paxman, and D. A. Carrara, "Comparison of phase diversity and curvature wavefront sensing," *Proc. SPIE* **3353**, pp. 930–940, 1998.
- 19. B. H. Dean and C. W. Bowers, "Diversity selection for phase-diverse phase retrieval," *J. Opt. Soc. Am. A* **20**, pp. 1490–1504, Aug 2003.

- 20. J. R. Fienup, J. C. Marron, T. J. Schulz, and J. H. Seldin, "Hubble space telescope characterized by using phase-retrieval algorithms," *Appl. Opt.* **32**, pp. 1747–1767, Apr 1993.
- 21. J. R. Fienup, "Phase-retrieval algorithms for a complicated optical system," *Appl. Opt.* **32**, pp. 1737–1746, Apr 1993.
- M. Guizar-Sicairos and J. R. Fienup, "Image reconstruction by phase retrieval with transverse translation diversity," Proc. SPIE 7076, p. 70760A, 2008.
- 23. A. S. Jurling and J. R. Fienup, "Phase retrieval with unknown sampling factors via the two-dimensional chirp z-transform," J. Opt. Soc. Am. A 31, pp. 1904–1911, Sep 2014.
- 24. R. Soummer, L. Pueyo, A. Sivaramakrishnan, and R. J. Vanderbei, "Fast computation of lyot-style coronagraph propagation," *Opt. Express* **15**, pp. 15935–15951, Nov 2007.